Rational Design and General Synthesis of S-Doped Hard Carbon with Tunable Doping Sites toward Excellent Na-Ion Storage Performance

Zhensheng Hong,* Yichao Zhen, Yurong Ruan, Meiling Kang, Kaiqiang Zhou, Jian-Min Zhang,* Zhigao Huang, and Mingdeng Wei

Heteroatom-doping is a promising strategy to tuning the microstructure of carbon material toward improved electrochemical storage performance. However, it is a big challenge to control the doping sites for heteroatom-doping and the rational design of doping is urgently needed. Herein, S doping sites and the influence of interlayer spacing for two kinds of hard carbon, perfect structure and vacancy defect structure, are explored by the first-principles method. S prefers doping in the interlayer for the former with interlayer distance of 3.997 Å, while S is doped on the carbon layer for the latter with interlayer distance of 3.695 Å. More importantly, one step molten salts method is developed as a universal synthetic strategy to fabricate hard carbon with tunable microstructure. It is demonstrated by the experimental results that S-doping hard carbon with fewer pores exhibits a larger interlayer spacing than that of porous carbon, agreeing well with the theoretical prediction. Furthermore, the S-doping carbon with larger interlayer distance and fewer pores exhibits remarkably large reversible capacity, excellent rate performance, and long-term cycling stability for Na-ion storage. A stable and reversible capacity of ≈200 mAh g^{-1} is steadily kept even after 4000 cycles at 1 A g^{-1}.

Rechargeable Li-ion batteries (LIBs), one of the most popular and mature energy storage technologies have been successfully utilized in various portable electronics in virtue of their high energy density and long cycle life.[1] However, many efforts have been so far devoted to the exploration of low cost and reliable

rechargeable battery systems beyond LIBs due to the rarity and non-uniform geographic distribution of Li resources.[2] Recently, Na-ion batteries (NIBs) with identical conception have been regarded as a potential battery technology for large-scale energy storage due to the abundant and ubiquitous sodium resources on earth compared to lithium.[2–8] However, many host materials for NIBs exhibited very limited capacity and sluggish diffusion kinetics toward Na-ion insertion due to the larger diameter of the Na-ion (1.02 Å) compared to Li-ion (0.76 Å). Now, a core issue for NIBs is designing and developing suitable anode materials with well reversible Na-ion insertion and extraction properties and satisfied capacity.[5–7]

To date, several types of Na-ion host anode materials have been demonstrated with acceptable capacity, mainly including alloy reaction material (Sn, Sb, and P),[9–11] conversion-type metal oxides and metal sulphides,[12–14] Ti-based intercalation compounds and carbonaceous materials.[15–23] Metallic alloys and conversion-type materials suffered from large volume expansion and poor electrochemical kinetics, while Ti-based compounds display relatively low reversible capacity. Therefore, carbonaceous materials are considered as the best option for considering their low cost and abundant resources, and thus receive lots of attention on developing novel carbon-based anode materials for NIBs in the past few years.[2,24–29] Graphite, the most commercial anode material in LIBs, can hardly storage Na-ion unless solvent cointercalation occurs, presumably due to the small interlayer distance (d_{002} = 0.334 nm).[20] Disordered or hard carbon appears to be the most suitable Na-ion host anode material for SIBs owing to the expanding interlayer distances and porous structure.[22–28] They are basically amorphous carbon composed of nanoscale domains of rumpled graphenic sheets with disordered structure along the *c*-axis.

It is worth mentioning that the introduction of covalent heteroatom-doping (N, B, P, S, etc.) to carbon materials has been proved to be a promising strategy to tuning their physicochemical properties, and thus delivering much improved electrochemical storage performance.[29–39] Nitrogen is the most commonly investigated heteroatom, while sulfur doping

Dr. Z. Hong, Y. Zhen, Y. Ruan, M. Kang, K. Zhou, Dr. J.-M. Zhang,
Prof. Z. Huang
Fujian Provincial Key Laboratory of Quantum Manipulation
and New Energy Materials College of Physics and Energy
Fujian Normal University
Fuzhou, Fujian 350117, China
E-mail: winter0514@163.com; jmzhang@fjnu.edu.cn
Dr. Z. Hong, Dr. J.-M. Zhang, Prof. Z. Huang
Fujian Provincial Collaborative Innovation Center for
Optoelectronic Semiconductors and Efficient Devices
Xiamen 361005, China
Prof. M. Wei
State Key Laboratory of Photocatalysis on Energy and Environment
Fuzhou University
Fuzhou 350002, China

The ORCID identification number(s) for the author(s) of this article can be found under https://doi.org/10.1002/adma.201802035.

in disordered or hard carbon is particularly interesting due to the significantly improved Na-ion storage capacity and rate capability.[34–39] Heteroatom-doping is also a familiar method to adjust the interlayer distances, which is a key point for Na-ion insertion activity especially for carbon anodes.[30,31,34–39] In these studies, various heteroatom-doped carbons with different interlayer distances were synthesized using different methods and different carbon sources. Unfortunately, they do not give a clear guide or general route to prepare carbon materials with enlarged interlayer distance by heteroatom-doping. Most studies for heteroatom-doping to nanocarbon materials are ascribed to so-called "topological defects," the doping sites and doping mechanism are far from elucidated. It is a very big challenge to control the doping sites in carbon material and develop a universal synthetic strategy.

In this work, two kinds of hard carbon, perfect structure and vacancy defect structure are proposed. Their S-doped positions and the influence of interlayer distance were explored by first-principles calculation. It is revealed that S prefers doping in the interlayer for hard carbon with perfect structure, while S doping occurs in vacancy defect sites on the carbon layer for defect structure, leading to the larger interlayer distance for the former under the same doping content. Furthermore, a general and one step molten salts method is developed to synthesize the hard carbons with different doping sites and interlayer distance. It is confirmed by experimental results that the S-doping hard carbon with fewer defects possesses a larger interlayer distance than that of porous carbon with lots of defects. Their interlayer distances are also corresponding well to the calculated results. Moreover, the S-doping carbon with fewer pores and larger interlayer distance exhibits a remarkable Na-ion storage performance due to the higher electrochemical activity and smaller barrier energy of Na diffusion.

In order to explore the S position and interlayer distance of S-doped hard carbon (initial interlayer distance = 3.50 Å), we calculate the formation energy of different S-doping configurations by the first-principles method. The internal coordinates of all the atoms are fully relaxed in evaluating the influences of different doping structures on the interlayer distance. The doping concentration of S atoms is 6.25% in the theoretical study, for a better comparison with the experiment results. First, we calculated three different S-doping positions (S1, S2, and Sz) for perfect hard carbon, as shown in **Figure 1**. From Table S1 of the Supporting Information, comparing the formation energy of S1, S2, and Sz, S2 with the lowest energy of 4.90 eV is energetically more stable than S1 and Sz by 0.16 and 6.1 eV, respectively. Therefore, S atom tends to be stable in the interlayer at the position S2 of pure hard carbon. The interlayer distance of S2 is 3.997 Å, corresponding with our experimental results, which would be discussed at the below text.

Then, we consider the S atom doping of hard carbon with vacancy defects. As shown in Figure S1 of the Supporting Information, all the possible positions (VS0, VS1, VS2, and VSz) for S atom are calculated. Figure S1a of the Supporting Information denotes that S atom just local in the vacancy defect site of hard carbon (VS0). Figure S1b,c of the Supporting Information shows the configurations of S doped near the vacancy defects (VS1 and VS2). The case that S absorbs in the layer with vacancy defect is described in Figure S1d of the Supporting Information. The calculated formation energy and interlayer distance are listed in Table S2 of the Supporting Information. Comparing the four configurations of S-doped hard carbon with vacancy defects, VS0 has the lowest formation energy of 4.50 eV, which clearly indicate that when the hard carbon has a vacancy defect, S atom tends to fill up at the vacancy defect site. In the case of VS0, the interlayer distance is 3.695 Å.

Based on the guide of theoretical calculation, we aim to design a synthetic method to prepare the hard carbon with different microstructures, as shown in **Figure 2**a. In this study, we used pitch as a carbon source due to the high carbon yield and low lost, which is very good source for the large scale production of carbon material.[40] S-doped hard carbon (S-HC-p) and S-doped porous hard carbon (S-PHC-p) from pitch were synthesized through the molten salts method by using sulfur and $Na_2S_2O_3$ powders as S sources, respectively. From the X-ray diffraction (XRD) patterns in Figure 2b, two broad peaks of (002) and (100) diffractions can be observed, which reveals a nongraphitic structure of carbons. More importantly, the remarkable increase of the average interlayer d-spacing for S-HC-p was clearly shown from the located position of the (002) diffraction peak compared with S-PHC-p. The d-spacing was up to 3.86 Å for S-HC-p, much larger than that of S-PHC-p (3.60 Å), calculated from the 2θ value by the Bragg's law. The sulfur content of both the carbon materials is around 6.3 at%, as shown in the Table S3 of
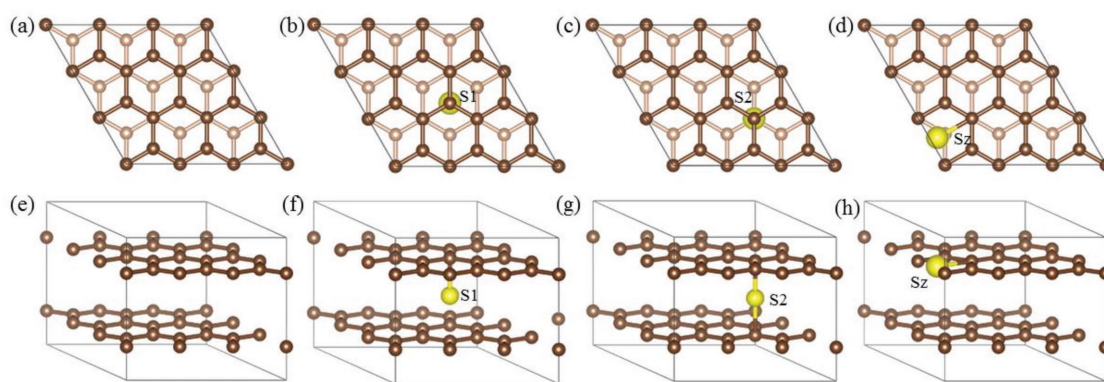

Figure 1. Crystal structures of: a) pure hard carbon, b,c) S-doped hard carbon with different sites (S1 and S2, respectively), d) S doped in the hard carbon layer (Sz). e–h) The side views of (a) to (d), respectively.
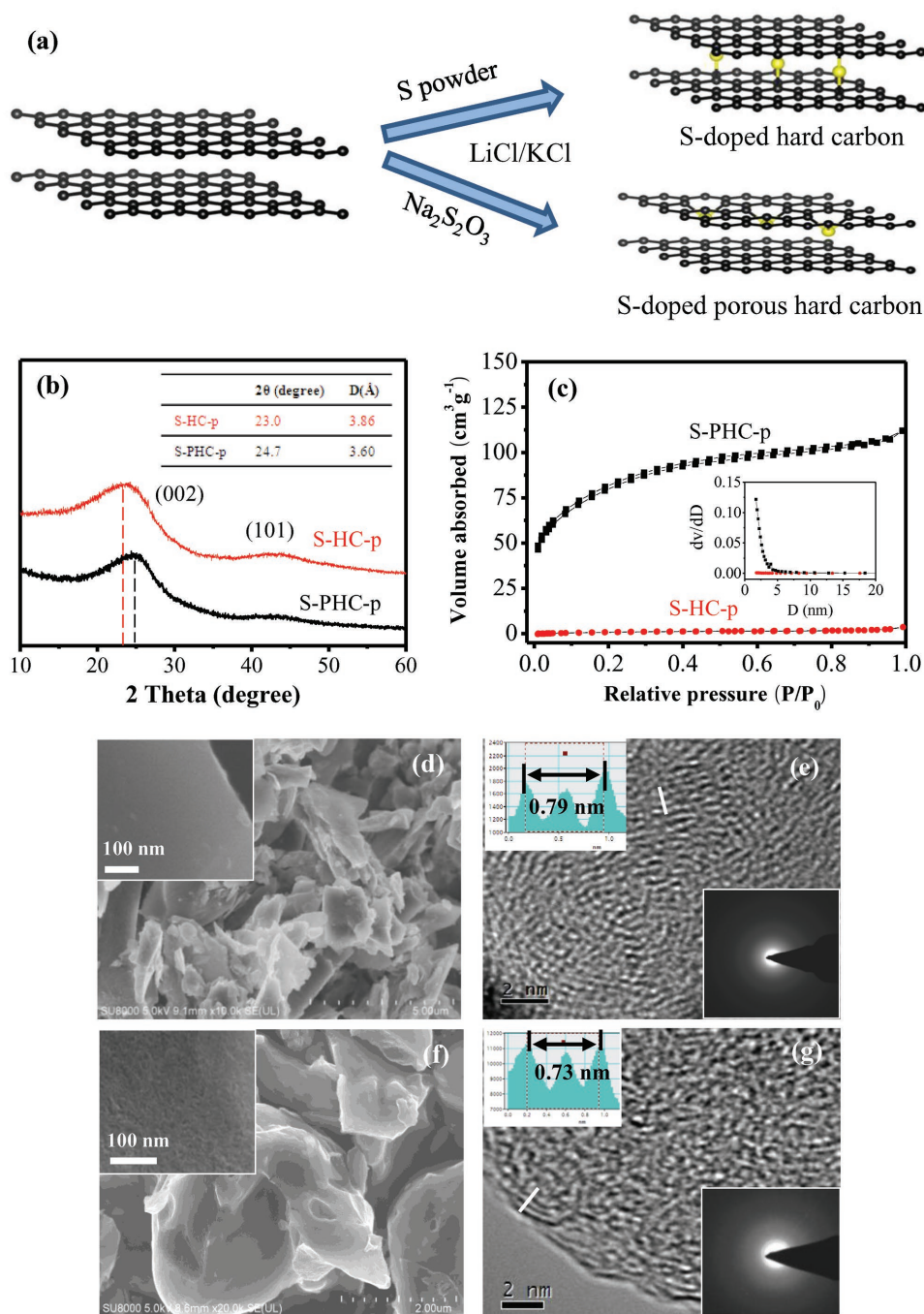
Figure 2. a) Schematic illustration of the synthesis of S-HC-p and S-PHC-p. b) XRD patterns of S-HC-p and S-PHC-p, inset is the interlayer distance between the (002) planes. c) Nitrogen adsorption–desorption isotherms of S-HC-p and S-PHC-p; the inset is the corresponding BJH size distribution of S-HC-p and S-PHC-p. d,f) SEM images of S-HC-p (d) and S-PHC-p (f), and the insets show the enlarged SEM images. e,g) HRTEM images of S-HC-p (e) and S-PHC-p (g), and the insets show the SAED patterns and corresponding intensity profiles for the line across the lattice fringes.

the Supporting Information. Besides, the *d*-spacing of pure HC is around 3.51 Å, as revealed from the XRD pattern (Figure S2, Supporting Information). Therefore, the experimental data of the average interlayer *d*-spacing as well as the sulfur content is coincident with the results of the theoretical calculation. N_2 adsorption–desorption isotherms measurements of the samples are shown in Figure 1c, demonstrating a much different

results for the two carbon materials. The Brunauer–Emmett–Teller (BET) surface area and the pore volume of S-PHC-p were determined to be 276.9 m^2 g^{-1} and 0.18 cm^3 g^{-1}, respectively. The BET surface are of S-HC-p is only 4.0 and pore structure in the material is barely present, and the comparable results are found for pure hard carbon (Figure S2, Supporting Information). Therefore, two different S-doped carbon materials, nearly

perfect structure and porous structure were successfully synthesized through a simple tuning of sulfur sources. In addition, the use of molten salts also has a significant effect on preparing the S-doped carbon materials with high purity, as revealed from the XRD pattern (Figure S3, Supporting Information) of the sample obtained from the direct solid state reaction.

The morphology and structure of the samples were revealed by scanning electron microscopy (SEM) and transmission electron microscopy (TEM) images as shown in Figure 2d–g. Both the carbon materials are found to have a nonuniform distribution of the particle size aound several micrometers. It is noted from Figure 2d (inset) that S-HC-p exhibits a smooth surface, while S-PHC-p possess a porous structure from Figure 2f (inset). This result is corresponding to the analysis of N_2 adsorption–desorption isotherms measurements. Figure 2e,g shows the high-resolution transmission electron microscopy (HRTEM) images of the different hard carbons, no obvious long-range ordered structure is observed in the two materials. Their selected area electron diffraction (SAED) patterns show dispersing diffraction rings, suggesting a further indication of amorphous structure. In addition, S-HC-p exhibits more the sharp diffraction rings than that of S-PHC-p, indicating more content of the graphitic domain structure. It should be notable that S-HC-p possesses a larger interlayer d-spacing (3.95 Å) compared with S-PHC-p (3.65 Å), which is coincident with the above XRD analysis.

Corresponding EDX elemental mapping C and S of S-HC-p and S-PHC-p are shown in Figure S4a,b of the Supporting Information, respectively. The homogeneous distribution of carbon and sulfur throughout the whole area of carbon material is clearly observed. Figure S4c of the Supporting Information shows the Raman spectra of the two samples, two separate characteristic bands of the D-band peak at 1346 cm^{-1} (the defect-induced band) and the G-band peak at 1590 cm^{-1} (the crystalline graphite band) are clearly observed.[29,41] The more intensive D-band peak for S-PHC-p indicates more defects compared with S-HC-p. Moreover, S-HC-p exhibits a larger value (1.08) of the intensity ratio of G-band to D-band (I_G/I_D) than that of S-PHC-p (0.99), suggesting a larger average domain size of graphenic layers. As presented in X-ray photoelectron spectroscopy (XPS) (Figure S4d, Supporting Information), three peaks at 163.8, 165.0, and 168.3 eV is observed for S 2p of S-HC-p, which can be attributed to S 2p3/2 and S 2p1/2 of C-S-C, C-SO$_x$, respectively.[29,38] The S 2p spectra for S-PHC-p (Figure S5, Supporting Information) also hold the same result. This corroborates the result that sulfur has been successfully doped into the carbon.

In order to examine the universal characteristics of the synthetic strategy, the common carbon source of glucose was used to fabricate carbon materials with tunable microstructure through the same method. As shown in Figure S6 of the Supporting Information, two kinds of carbon materials with different structures were successfully synthesized. S-HC-g possesses a larger interlayer distance (3.99 Å) than that of S-PHC-g (3.70 Å), while the latter exhibits a porous structure and larger surface area. There morphology and structure were also characterized by SEM and HRTEM images, as presented in Figure S7 of the Supporting Information. Numerous and uniform nanosheets with average size of several hundred nanometers are found for S-HC-g from Figure S7a of the Supporting Information, and a relative smooth surface is observed. S-PHC-g

(Figure S7c, Supporting Information) also displays nanosheet morphology, but has a smaller thickness and porous structure compared with S-HC-g. Figure S7c,d of the Supporting Information shows the HRTEM images of S-HC-g and S-PHC-g, respectively. It is revealed that S-HC-g has a larger interlayer distance (4.0 Å) than that of S-PHC-g (3.7 Å), which confirm the results of XRD analysis. The Raman spectra (Figure S8a, Supporting Information) and XPS spectra (Figure S8b–d, Supporting Information) also uncover the similar results with the carbon made from pitch.

Based on the prediction from first-principles calculation, S atom tends to be stable in the interlayer at the position S2 (see Figure 1) in hard carbon with perfect structure, leading to an interlayer distance 3.997 Å under the doping concentration of 6.25%. On the other hand, S atom prefers to filling up at the vacancy defect site of VS0 (see Figure S1, Supporting Information) in hard carbon with vacancy defect structure, and thus possess a interlayer distance of 3.695 Å. Under the guide of theoretical prediction, we chose $Na_2S_2O_3$ and S powders as S resources to synthesize S-doped hard carbon with different microstructures. During the formation of C−S−C bonds, $S_2O_3^{2-}$ would be reduced by carbon accompanied with the yield of C−O gas, resulting to the formation of porous structure in the final carbon material. This result was also found by Liu and Antonietti,[42] and other sulfate could also be used to prepare porous S-doped carbon. As to S power, it can be sublimed to gaseous state with high reactivity at high temperature, which could be make for relative direct doping and allowing the formation of hard carbon with few pores. Finally, S-doping would occur at different sites due to the formation of two kinds of hard carbons with different doping mechanisms. Therefore, the theoretical prediction is well conformed by experimental results. In the past few years, although various heteroatom-doped carbon materials were prepared, S-doped hard carbon with low surface area or fewer defects and high doping level is scarcely reported. More importantly, the fabrication of S-doped carbon materials with tunable doping sites were not achieved and elucidated before.

Finally, the sodium storage properties of the carbon with different microstructures were investigated by Na-ion half-cells. Galvanostatic charge–discharge profiles of different carbon electrodes at 0.05 A g^{-1} in the potential window of 0.01–3.0 V are shown in **Figure 3**a,b. Although they display a comparable discharge capacity around 870 mAh g^{-1} at the first cycle, S-HC-p has a larger charge (reversible) capacity of 488 mAh g^{-1} than that of S-PHC-p (432 mAh g^{-1}), suggesting a better first initial Coulombic efficiency (56%) for the carbon with larger interlayer distance. In addition, Figure S9a of the Supporting Information exhibits the discharge and charge profiles of pure hard carbon with a small surface area and low degree of pore defects, the initial Coulombic efficiency for this material is only 42%. It is noted that a slope in the range of 1–1.3 V can be observed for S-HC-p, while this is not identified for S-PHC-p and HC. CV curves (Figure S9, Supporting Information) also confirm this result, which demonstrated that S-HC-p exhibits much higher electrochemical reactivity with more apparent redox peaks than that of S-PHC-p and HC. In addition, the large irreversible capacity loss for electrode in the initial cycle can be ascribed to the formation of solid electrolyte interphase film. The irreversible
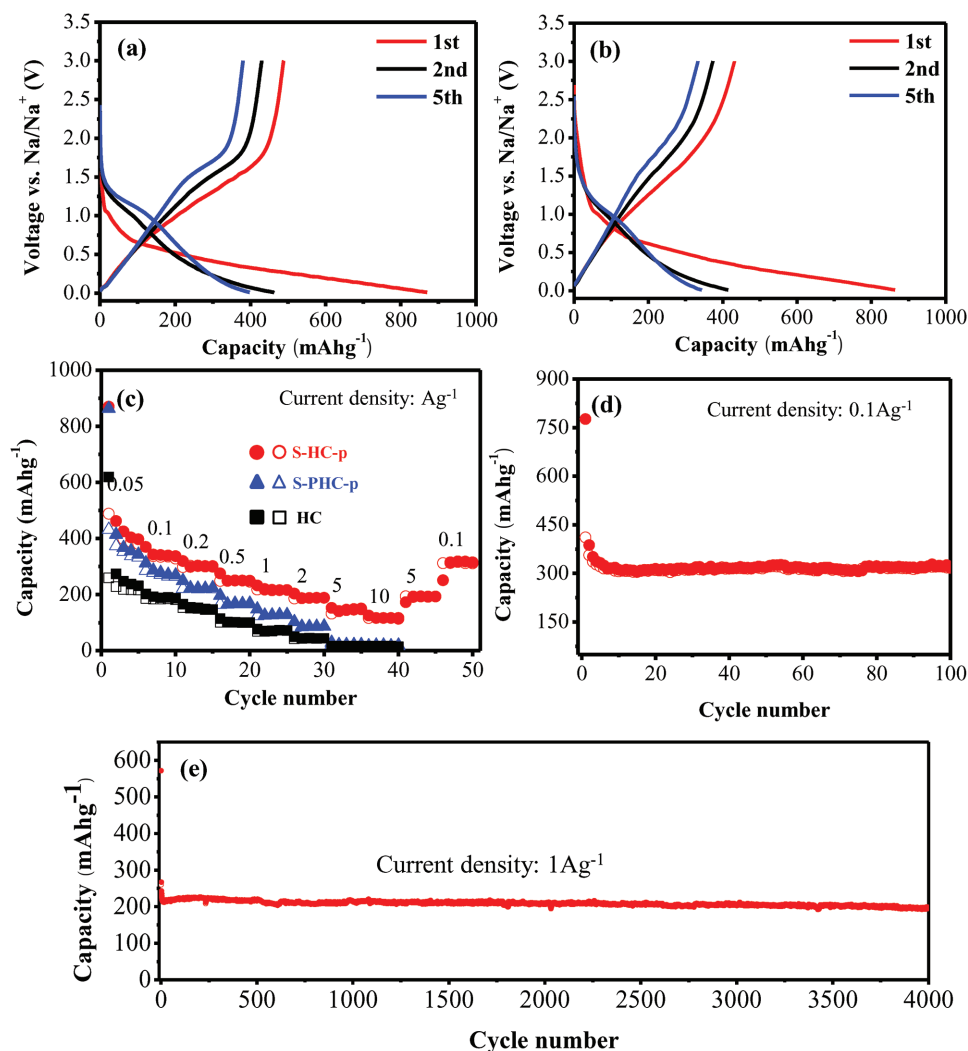
**ADVANCED
SCIENCE NEWS**

www.advancedsciencenews.com

**ADVANCED
MATERIALS**

www.advmat.de

Figure 3. Discharge and charge profiles for the 1st, 2nd, and 5th cycles of: a) S-HC-p and b) S-PHC-p at a rate of 0.05 A g^{-1}. c) Rate capability for the three hard carbon electrodes at various current densities for 5 cycles. d) Cycling performance of S-HC-p and S-PHC-p at 0.1 A g^{-1}. e) Long cycling stability of S-HC-p electrode at a constant current density of 1 A g^{-1}.

capacity caused by side reactions was also observed from CV curves at the first cycle. Therefore, the large surface area or porous structure is not the exclusive reason for the irreversible capacity, which were considered as the domain reason in the previous study.[29,43] It is notable that the S-doped hard carbon in this study is prepared under a low temperature, the crystallinity is lower than the typical hard carbon in the literature obtained at high sintering temperature.[22,24,28] It is suggested that the relative low electronics transport in hard carbon is also a reason for the irreversible capacity. As depicted by electrochemical impedance spectroscopy (EIS) (Figure S10, Supporting Information), the hard carbon electrodes have a relative large resistance, and the low electricity may induce more side reactions. This phenomenon was also found in TiO$_2$ anode for NIBs.[17]

Figure 3c describes the rate capability of two electrodes at various current densities. The rate performance of S-HC-p is much superior compared with S-PHC-p, and reversible average capacities of 420, 340, 300, 250, 217, 189, and 145 mAh g^{-1} were obtained at 0.05, 0.1, 0.2, 0.5, 1, 2, and

5 A g^{-1}, respectively. More excitingly, a stable capacity of about 117 mA g^{-1} can be remained even at a very high current density of 10 A g^{-1}. Moreover, the reversible capacity can be reverted when returned to low current densities. Therefore, the reversible capacity and rate performance is higher than or comparable with most S-doped hard carbons.[34–39] S-HC-p shows good cycling performance, as shown in Figure 3d. A stable capacity of 320 mAh g^{-1} for S-HC-p was obtained after 100 cycles at 0.1 A g^{-1}. The long-term cycling performance of the S-HC-p at a high current density of 1 A g^{-1} was further evaluated, as shown in Figure 3e. A reversible capacity of ≈200 mAh g^{-1} was maintained even after 4000 cycles, indicating the excellent durability of the S-HC-p electrode. The excellent Na-ion storage performance combining with the high yield and low lost makes S-HC-p become one of the most promising anode materials for NIBs.

The sodium storage properties of the hard carbon made from glucose were also studied. The charge–discharge profiles of the electrodes were presented in Figure S11a,b of the Supporting

Information. S-PHC-g electrode delivers a large first discharge (1408 mA g^{-1}) and charge capacity (788 mA g^{-1}), which could be due to the prodigious surface area (994.8 m² g^{-1}). However, the cycling stability and rate performance are poor for S-PHC-g electrode. As a comparison, S-HC-g electrode exhibits remarkable rate capability (Figure S11c, Supporting Information), and reversible average capacities of 430, 374, 340, 298, 270, 244, 208, and 175 mAh g^{-1} were obtained at 0.05, 0.1, 0.2, 0.5, 1, 2, 5, and 10 A g^{-1}, respectively. To the best of our knowledge, this is the best rate performance for hard carbon materials up to now. Figure S10d of the Supporting Information shows the cycling performance of S-HC-g, a reversible capacity of 380 mAh g^{-1} were remained after 100 cycles at 0.1 A g^{-1}. More exciting, a stable and reversible capacity of ≈240 mAh g^{-1} was steadily kept even after 2000 cycles at a high current rate of

1 A g^{-1} (Figure S11e, Supporting Information), indicating the excellent cycling stability of the S-HC-g electrode.

The Na-ion storage for S-PHC-p and HC is mainly from capacitive charge storage by surface adsorption/desorption of ions surface adsorption/desorption of ions based on the CV curves and the charge/discharge profiles without obvious plateau. Na-ion storage mechanism for S-HC-p is undertaken using CV and the time-dependent electrochemical response, which obeys a power-law relationship, $i = av^{\beta}$. Here, i and v is the peak current and sweep, a and b are adjustable constants. If b-value approaches 1, the electrochemical process is mainly controlled by capacitance, and the battery behavior dominates when the b-value is close to 0.5. **Figure 4**a,b shows CV curves of at various sweep rates from 0.1 to 2 mV s^{-1} and derived relationship between the peak currents and scan rates
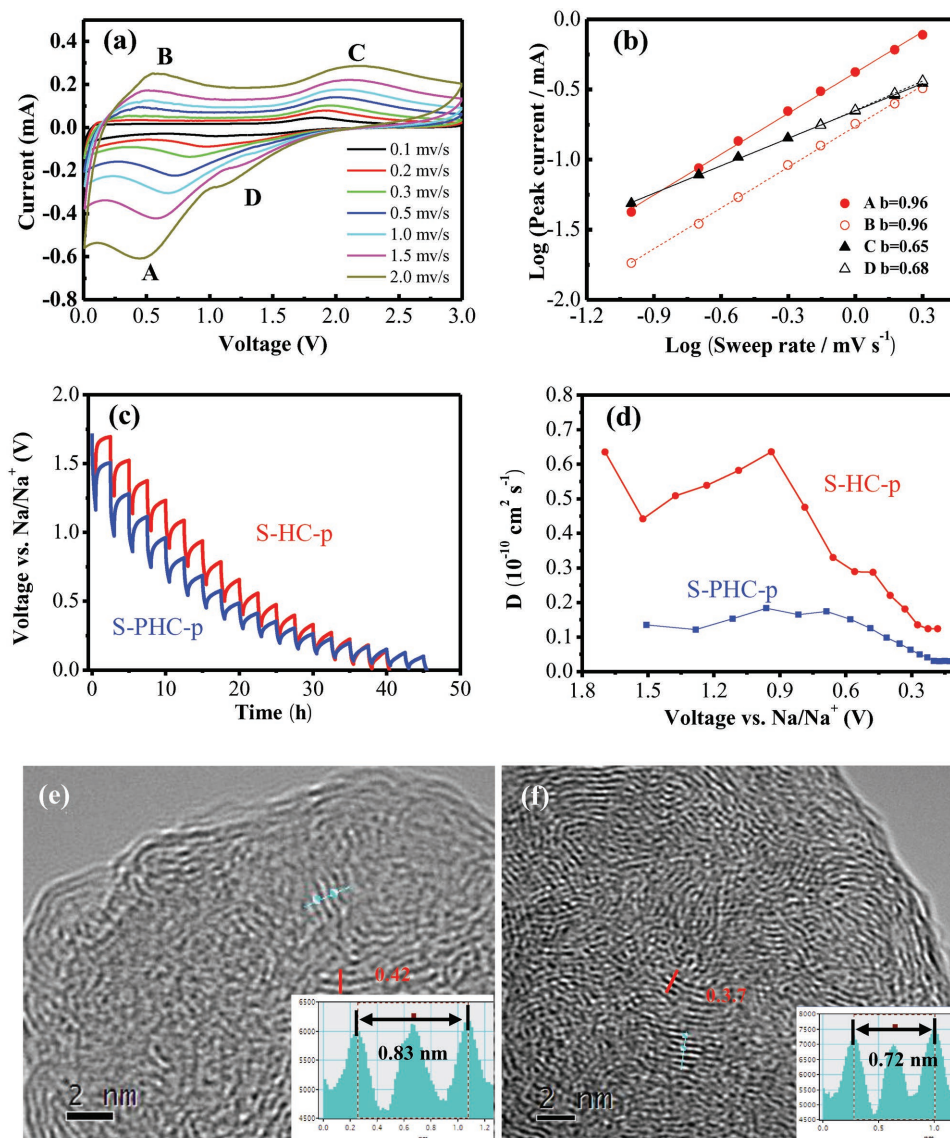

Figure 4. a) Cyclic voltammetry curves of S-HC-p at various sweep rates from 0.1 to 2 mV s^{-1} and b) the derived relationship between the peak currents and scan rates in logarithmic format. c) GITT potential profiles of the two electrodes for sodiation process during the second cycle and d) Na-ion diffusion coefficients calculated from the GITT potential profiles. e,f) HRTEM images of S-HC-p (e) and S-PHC-p (f) after discharging to 0.01 V, and the insets show the corresponding intensity profiles for the line across the lattice fringes.

in logarithmic format. As the *b*-value approaches 1 for A and B peaks, suggesting the Na-ion storage process in this region is mainly controlled a pseudo-capacitive process. However, the *b*-value for C and D peaks is less than 0.7, indicating an insertion behavior domain process. Thus, it is an interesting finding that two kinds of charge storage mechanism are concurrent for S-HC-p. Galvanostatic intermittent titration technique (GITT) was employed to measure the apparent diffusion coefficient of Na-ion in hard carbon electrodes with a pulse current at 0.05 A g^{-1} for 0.5 h between rest intervals for 2 h. The diffusivity coefficient can be estimated according to Fick's second law as follows

$$D = \frac{4}{\pi \tau} \left(\frac{m_B V_M}{M_B S} \right)^2 \left(\frac{\Delta E_s}{\Delta E_\tau} \right)^2 \tag{1}$$

Here, τ is the pulse duration, M_B is molar mass of carbon, m_B and S are the active mass and surface area for the tested electrode, V_M is the molar volume, ΔE_S and ΔE_τ can be obtained from the GITT profiles. As depicted in Figure 4c,d, the two hard carbons have similar diffusivity coefficient variation, but S-HC-p exhibit much larger diffusivity coefficient during entire sodiation process and desodiation process (Figure S12, Supporting Information). HRTEM images of the eletrodes after discharged to 0.01 V reveal the the structural changes during sodiation process, as shown in Figure 4e,f. The interlayer spacing of S-HC-p is enlared to around 0.42 nm, which is nearly not charged for S-PHC-p. This finding further reveal

the higher Na-ion storage capability for S-HC-p as supported by GITT results, and suggests that interlayer spacing is a key factor for the Na-ion storage in hard carbon.

To further explore the performance of S atom in hard carbon, we evaluate the different interlayer distances and S-doped (site S2) on the Na diffusion barrier and electronic conductivity by first-principles calculation. First, the diffusion path for undoped carbon is shown in **Figure 5**a. The results of the barrier energy as shown in Figure S6c of the Supporting Information, we can see the effect of interlayer distance on barrier energy. The results indicate that the interlayer distance increases from 3.5 to 3.9 Å and the corresponding barrier energy decreases from 392 to 164 meV. Second, we calculate the barrier energy of Na diffusion in the most stable S-doped hard carbon with an interlayer distance of 3.9 Å (S2), the diffusion path as shown in Figure 5b. Form Figure 5c, the barrier energy reduced from 164 to 130 meV through S doping. The results show that S doping can reduce the diffusion barrier of Na and make the diffusion of Na easier. Finally, the density of states of S doped (initial interlayer distance = 3.5 Å, site S2) and undoped hard carbon is show in Figure 5d. Compared to undoped hard carbon, the S-doped hard carbon has no bandgap and possesses rich electrons at the Fermi level. The result suggests that the electronic conductivity of S-doped hard carbon is enhanced. From the above results, the expanded interlayer distance and S-doped hard carbon can lead to a decrease in the diffusion barrier energy of Na. On the other hand, S-doped enhanced electronic conductivity promotes faster transport of electrons. Therefore,
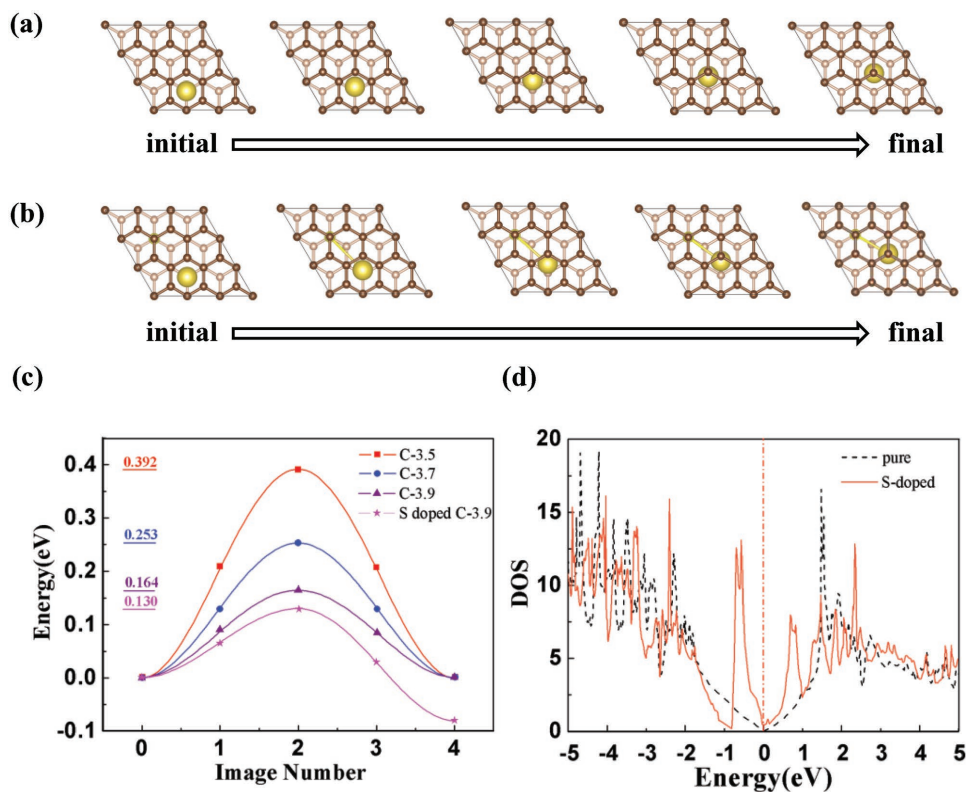

Figure 5. The minimum energy path for one Na atom diffusion from one hollow site to the nearest hollow site in: a) pure (interlayer distance 3.5, 3.7, and 3.9 Å), and b) S-doped hard carbon (site S2). c) Different interlayer distances and S doping barrier energy. d) Density of states (DOS) of the pure and S-doped hard carbon (initial interlayer distance = 3.5 Å, site S2). The Fermi level is set at zero.

**ADVANCED
SCIENCE NEWS**

www.advancedsciencenews.com

**ADVANCED
MATERIALS**

www.advmat.de

S-doped hard carbon can significantly enhance the mobility of Na and the electronic conductivity, which can effectively improve the Na-ion storage performance.

In summary, S-doped sites and the influence of interlayer distance for hard carbon with perfect structure and vacancy defect structure were studied by first-principles calculation. Our theoretical calculation predicts that S prefers doping in the interlayer for hard carbon with perfect structure, while S doping takes place in vacancy defect sites with defect structure, and thus the former has a larger interlayer distance than that of latter. More exciting, a universal and facile synthetic method is provided to prepare hard carbon with different microstructures and interlayer distances. The experimental results confirm that S-doping hard carbon with fewer defects possesses a larger interlayer distance than that of porous carbon with lots of defects. Their interlayer distances are also corresponding well to the calculated results, indicating the achievement of the same doping sites with theoretical prediction. Furthermore, the S-doping carbon with larger interlayer distance and smaller surface area exhibits remarkable large reversible capacity, excellent rate performance, and long-term cycling durability due to the much smaller barrier energy of Na diffusion. This study not only brings an in-depth comprehension and guide for designing heteroatom-doped carbon materials, but also provides a general synthetic method for the fabrication of carbon materials with excellent electrochemical storage performance.

Supporting Information

Supporting Information is available from the Wiley Online Library or from the author.

Conflict of Interest

The authors declare no conflict of interest.

[1] B. Dunn, H. Kamath, J.-M. Tarascon, *Science* **2011**, *334*, 928.
[2] D. Larcher, J. M. Tarascon, *Nat. Chem.* **2015**, *7*, 19.
[3] J.-Y. Hwang, S.-T. Myung, Y.-K. Sun, *Chem. Soc. Rev.* **2017**, *46*, 3529.
[4] W. Luo, F. Shen, C. Bommier, H. Zhu, X. Ji, L. Hu, *Acc. Chem. Res.* **2016**, *49*, 231.
[5] M. Á. Muñoz-Márquez, D. Saurel, J. L. Gómez-Cámer, M. Casas-Cabanas, E. Castillo-Martínez, T. Rojo, *Adv. Energy Mater.* **2017**, *7*, 1700463.
[6] N. Yabuuchi, K. Kubota, M. Dahbi, S. Komaba, *Chem. Rev.* **2014**, *114*, 11636.
[7] D. Kundu, E. Talaie, V. Duffort, L. F. Nazar, *Angew. Chem., Int. Ed.* **2015**, *54*, 3431.
[8] H.-G. Wang, W. Li, D.-P. Liu, X.-L. Feng, J. Wang, X.-Y. Yang, X.-b. Zhang, Y. Zhu, Y. Zhang, *Adv. Mater.* **2017**, *29*, 1703012.
[9] M. Lao, Y. Zhang, W. Luo, Q. Yan, W. Sun, S. X. Dou, *Adv. Mater.* **2017**, *29*, 1700622.
[10] Y. Liu, N. Zhang, L. Jiao, J. Chen, *Adv. Mater.* **2015**, *27*, 6702.
[11] W. Li, S. Hu, X. Luo, Z. Li, X. Sun, M. Li, F. Liu, Y. Yu, *Adv. Mater.* **2017**, *29*, 1605820.
[12] N. Zhang, X. Han, Y. Liu, X. Hu, Q. Zhao, J. Chen, *Adv. Energy Mater.* **2015**, *5*, 1401123.
[13] X. Xu, C. Niu, M. Duan, X. Wang, L. Huang, J. Wang, L. Pu, W. Ren, C. Shi, J. Meng, B. Song, L. Mai, *Nat. Commun.* **2017**, *8*, 460.
[14] P. He, Y. Fang, X.-Y. Yu, X. W. Lou, *Angew. Chem., Int. Ed.* **2017**, *56*, 12202.
[15] M. N. Tahir, B. Oschmann, D. Buchholz, X. Dou, I. Lieberwirth, M. Panthöfer, W. Tremel, R. Zentel, S. Passerini, *Adv. Energy Mater.* **2016**, *6*, 1501489.
[16] J. Ni, S. Fu, C. Wu, J. Maier, Y. Yu, L. Li, *Adv. Mater.* **2016**, *28*, 2259.
[17] Z. Hong, M. Kang, X. Chen, K. Zhou, Z. Huang, M. Wei, *ACS Appl. Mater. Interfaces* **2017**, *9*, 32071.
[18] P. Senguttuvan, G. Rousse, M. E. Arroyo y de Dompablo, H. Vezin, J. M. Tarascon, M. R. Palacín, *J. Am. Chem. Soc.* **2013**, *135*, 3897.
[19] Y. Wen, K. He, Y. Zhu, F. Han, Y. Xu, I. Matsuda, Y. Ishii, J. Cumings, C. Wang, *Nat. Commun.* **2014**, *5*, 4033.
[20] B. Jache, P. Adelhelm, *Angew. Chem., Int. Ed.* **2014**, *53*, 10169.
[21] D. A. Stevens, J. R. Dahn, *J. Electrochem. Soc.* **2001**, *148*, A803.
[22] S. Komaba, W. Murata, T. Ishikawa, N. Yabuuchi, T. Ozeki, T. Nakayama, A. Ogata, K. Gotoh, K. Fujiwara, *Adv. Funct. Mater.* **2011**, *21*, 3859.
[23] Y. Cao, L. Xiao, M. L. Sushko, W. Wang, B. Schwenzer, J. Xiao, Z. Nie, L. V. Saraf, Z. Yang, J. Liu, *Nano Lett.* **2012**, *12*, 3783.
[24] Y. Li, Y.-S. Hu, M.-M. Titirici, L. Chen, X. Huang, *Adv. Energy Mater.* **2016**, *6*, 1600659.
[25] Y. Zheng, Y. Wang, Y. Lu, Y.-S. Hu, J. Li, *Nano Energy* **2017**, *39*, 489.
[26] F. A. Soto, P. Yan, M. H. Engelhard, A. Marzouk, C. Wang, G. Xu, Z. Chen, K. Amine, J. Liu, V. L. Sprenkle, F. El-Mellouhi, P. B. Balbuena, X. Li, *Adv. Mater.* **2017**, *29*, 1606860.
[27] J. He, N. Wang, Z. Cui, H. Du, L. Fu, C. Huang, Z. Yang, X. Shen, Y. Yi, Z. Tu, Y. Li, *Nat. Commun.* **2017**, *8*, 1172.
[28] L. Xiao, Y. Cao, W. A. Henderson, M. L. Sushko, Y. Shao, J. Xiao, W. Wang, M. H. Engelhard, Z. Nie, J. Liu, *Nano Energy* **2016**, *19*, 279.
[29] H. Hou, X. Qiu, W. Wei, Y. Zhang, X. Ji, *Adv. Energy Mater.* **2017**, *7*, 1602898.
[30] Q. Xia, H. Yang, M. Wang, M. Yang, Q. Guo, L. Wan, H. Xia, Y. Yu, *Adv. Energy Mater.* **2017**, *7*, 1701336.
[31] Y. Yang, D.-M. Tang, C. Zhang, Y. Zhang, Q. Liang, S. Chen, Q. Weng, M. Zhou, Y. Xue, J. Liu, J. Wu, Q. H. Cui, C. Lian, G. Hou, F. Yuan, Y. Bando, D. Golberg, X. Wang, *Energy Environ. Sci.* **2017**, *10*, 979.
[32] M. Wang, Y. Yang, Z. Yang, L. Gu, Q. Chen, Y. Yu, *Adv. Sci.* **2017**, *4*, 1600468.
[33] Y. Xie, Y. Chen, L. Liu, P. Tao, M. Fan, N. Xu, X. Shen, C. Yan, *Adv. Mater.* **2017**, *29*, 1702268.
[34] W. Li, M. Zhou, H. Li, K. Wang, S. Cheng, K. Jiang, *Energy Environ. Sci.* **2015**, *8*, 2916.
[35] F. Pei, T. An, J. Zang, X. Zhao, X. Fang, M. Zheng, Q. Dong, N. Zheng, *Adv. Energy Mater.* **2016**, *6*, 1502539.
[36] G. Zou, C. Wang, H. Hou, C. Wang, X. Qiu, X. Ji, *Small* **2017**, *13*, 1700762.

ADVANCED
SCIENCE NEWS

www.advancedsciencenews.com

ADVANCED
MATERIALS

www.advmat.de

[37] J. Yang, X. Zhou, D. Wu, X. Zhao, Z. Zhou, *Adv. Mater.* **2017**, *29*, 1604108.

[38] D. Xu, C. Chen, J. Xie, B. Zhang, L. Miao, J. Cai, Y. Huang, L. Zhang, *Adv. Energy Mater.* **2016**, *6*, 1501929.

[39] Z. Li, C. Bommier, Z. S. Chong, Z. Jian, T. W. Surta, X. Wang, Z. Xing, J. C. Neuefeind, W. F. Stickle, M. Dolgos, P. A. Greaney, X. Ji, *Adv. Energy Mater.* **2017**, *7*, 1602894.

[40] Y. Li, Y.-S. Hu, H. Li, L. Chen, X. Huang, *J. Mater. Chem. A* **2016**, *4*, 96.

[41] M. S. Dresselhaus, A. Jorio, M. Hofmann, G. Dresselhaus, R. Saito, *Nano Lett.* **2010**, *10*, 751.

[42] X. Liu, M. Antonietti, *Adv. Mater.* **2013**, *25*, 6284.

[43] S. Huang, Z. Li, B. Wang, J. Zhang, Z. Peng, R. Qi, J. Wang, Y. Zhao, *Adv. Funct. Mater.* **2018**, *28*, 1706294.

1802035 (9 of 9)